Variability of Deep-Ocean Mass Transport: Spectral Shapes and Spatial Scales

JIN-SONG VON STORCH

Institute of Meteorology, University of Hamburg, Hamburg, Germany

PETER MÜLLER

Department of Oceanography, University of Hawaii, Honolulu, Hawaii

RONALD J. STOUFFER

Geophysical Fluid Dynamics Laboratory, NOAA, Princeton, New Jersey

REINHARD VOSS

German Climate Computer Center, Hamburg, Germany

SIMON F. B. TETT

Hadley Centre, U.K. Meteorological Office, Bracknell, Berkshire, United Kingdom

(Manuscript received 19 June 1998, in final form 18 May 1999)

ABSTRACT

This paper studies the variability of deep-ocean mass transport using four 1000-yr integrations performed with coupled general circulation models. Statistics describing the spectral and spatial features are considered. It is shown that these features depend crucially on the time-mean state. For the transport of tropical and subtropical water masses in three of the integrations, the spectral levels continually increase with decreasing frequency and do not show isolated peaks at low frequencies. The slope of the low-frequency spectrum (in a log–log plot) changes with increasing depth. It has values of about 0 near the surface, about -1 at intermediate depth, and about -2 at or near the bottom. The result indicates that the maximal memory timescale for deep-ocean mass transport is longer than a few centuries. The situation is different in the fourth integration, which has a different mean circulation pattern. In this case, the low-frequency spectrum is more or less flat in the tropical and subtropical oceans below 2000–3000 m, indicating weak low-frequency variations. The dominant spatial covariance structures describe an anomalous recirculation of intermediate water masses, which is confined to a large extent to each ocean basin. The spatial scale of the dominant modes is therefore smaller than that of the time-mean circulation.

1. Introduction

Very little is known about the variability of the present-day thermohaline circulation. This is caused not only by the scarcity of the observational data for the deep ocean but also by the shortage of computer power in running fully coupled atmosphere–ocean general circulation models (GCMs) over time periods of thousands of years. The computationally less expensive ocean-only GCMs are generally used to study the mean state of the deep ocean, in particular the causes of changes in the mean state, such as multiple equilibria of the thermohaline circulation. However, as pointed out by Hasselmann (1976), ocean-only GCMs that do not include weather events cannot provide information about *the variability around the mean.* Although weather noise can be included by imposing stochastic components into the mean boundary forcing, the full richness of the atmospheric variability including its feedbacks and from that the full spectrum of variability of the deep ocean can be realistically generated only by actively coupled atmosphere–ocean GCMs.

Up to now, only a few 1000-yr integrations with coupled GCMs have been carried out (Manabe and Stouffer 1996; Tett et al. 1997; Voss et al. 1998; Cubasch et al. 1992; von Storch et al. 1997). The integrations were performed at the Geophysical Fluid Dynamics Labo-

Corresponding author address: Dr. Jin-Song von Storch, Meteorologisches Institut, Universität Hamburg, Bundesstrasse 55, D-21046 Hamburg, Germany.
E-mail: jin@gkss.de

ratory (Princeton, New Jersey), the Max Planck Institute for Meteorology (Hamburg, Germany), the German Climate Computer Center (Hamburg, Germany), and the Hadley Centre (Bracknell, United Kingdom), and will be referred to as the GFDL, ECHAM1/LSG, ECHAM3/LSG, and HadCM2 runs, respectively. Some of the runs have been performed with the goal of producing unperturbed control integrations for global warming studies. All four integrations were carried out with flux corrections. All of the coupled GCMs have coarse resolution and do not simulate mesoscale oceanic variations. Despite these problems, the coupled integrations provide an academic framework in which the deep ocean is modeled likely not in a completely realistic but in a dynamically consistent manner. Within such a framework, this paper studies variations obtained from runs with different time-mean states. The mean oceanic state itself is not the subject of this paper and will not be considered in detail.

Two properties of the deep-ocean variability are studied. The first one concerns the spectral characteristics. Emphasis is put on spectral shapes that might be described by power laws rather than on spectral values at particular frequencies. Studies concerning spectral shapes of oceanic variability have been mainly concentrated on variables of the upper ocean, such as those describing (baroclinic) Rossby waves. A recent study by Frankignoul et al. (1997) showed that the spectra of these variables reveal an ω^{-2} shape (where ω is frequency) at high frequencies and level off at frequencies lower than one cycle every few decades. The variables describing Rossby waves cannot, however, be used to characterize transport of water masses, which is the subject of this paper.

The second aspect concerns the typical spatial scale of the variability. For the atmosphere, it is known that the dominant variability, such as synoptic disturbances or teleconnectivity, has much smaller spatial scales than the mean circulation, which is characterized by the global-scale distribution of jets. The present-day deep-ocean circulation, characterized as the ''conveyor belt'' by Broecker (1991) and summarized recently by Schmitz (1995), has a global cross-basin scale. The questions of how the dominant modes of the variability of deep-ocean mass transport look and whether they also have cross-basin spatial scales are still open and will be considered here.

The analysis is based on the zonally averaged streamfunctions, which exclude the effects of waves and characterize transports of water masses. Meridional–vertical sections of the global ocean and of each ocean basin are considered. The latter extend to about 30°S, where the meridional boundaries of the oceans end. Yearly time series of the four integrations are used. To limit the number of diagrams, results from the analysis of the Indian Ocean and some of the global ocean are not displayed. For the integrations with the HadCM2 and ECHAM1/LSG models, which extend to 1592 and 1260 yr respectively, only the last 1000 yr are analyzed. The integrations of the ECHAM3/LSG and GFDL models are still running. In this case, the first 1000 yr are considered. Section 2 gives a brief description of the four coupled models and the four 1000-yr integrations performed with these models. The difference between the mean thermohaline circulations in these models is discussed. Statistical properties of the deep-ocean variability concerning the spectral form and spatial scales are discussed in sections 3 and 4, respectively. A conclusion is given in the final section.

2. The 1000-yr integrations

a. Model descriptions

Descriptions of the four coupled models and integrations with these models can be found in Manabe and Stouffer (1996), Manabe et al. (1991), Voss et al. (1998), Voss (1996), Cubasch et al. (1992), von Storch et al. (1997), Tett et al. (1997), and Johns et al. (1997). As this paper focuses on the transports of deep water masses, some features of the oceanic components of the coupled models that can potentially affect the formation and transport of water masses are summarized in Table 1.

Two types of ocean models are used in the four integrations. The LSG ocean model is designed to represent large-scale, geostrophic motions (Hasselmann 1982; Maier-Reimer et al. 1993). The physical features of the LSG versions in the ECHAM3/LSG and ECHAM1/LSG runs are identical. Differences between the two runs are induced by different atmospheric GCMs and the different spinup procedures. The ocean components of the HadCM2 model and the GFDL model are both based on the Bryan–Cox primitive equation model (Bryan 1969; Cox 1984). Further refinements are included in the HadCM2 model. For instance, an energy balance mixed layer model based on Kraus and Turner (1967) is embedded in the HadCM2 model. The HadCM2 model has the finest resolution among the considered models.

For the four integrations considered, different spinup runs are carried out to bring the oceans to their equilibrium states before coupling them with the atmosphere. Apart from different formulations, the different spinup runs may also cause differences in the time-mean circulations and in the variability of the deep oceans. Two types of spinup integrations are carried out. The GFDL and the two ECHAM/LSG runs are performed using an ocean-only model, whereas the HadCM2 run is carried out in a coupled mode.

The ECHAM1/LSG spinup run is done by integrating the ocean-only model for 7000 yr. The boundary forcing changes from restoring conditions for temperature and salinity (restoring to the observed values) in the first 5000 yr to mixed-boundary conditions in the last 2000 yr. The freshwater fluxes of the mixed-boundary conditions are diagnosed from the first 5000 yr. For the

TABLE 1. Summary of main features of the oceanic components of the coupled models.

	GFDL	ECHAM3/LSG	ECHAM1/LSG	HadCM2
(Effective) resolution	4.5° × 3.75°	4° × 4°	As ECHAM3/LSG	2.5° × 3.75°
No. of vertical levels	12	11	As ECHAM3/LSG	20
Basic equations	Complete set of primitive equations	Primitive equations, neglecting nonlinear advection of momentum	As ECHAM3/LSG	As GFDL
Approximations	Hydrostatic, Boussinesq, rigid lid	Hydrostatic, Boussinesq	As ECHAM3/LSG	As GFDL
Vertical diffusion [order of magnitude (m^2 s^{-1})]	0.3–1.3 × 10^{-4} with maximal value at the bottom	~10^{-4} for deep ocean (through an upwind discretization method)	As ECHAM3/LSG	0.1–1.5 × 10^{-4} with maximal value at the bottom
Spinup	2400 yr in an uncoupled mode, 34 000 yr for deep ocean using an acceleration technique (Bryan 1984)	27 000 yr in an uncoupled mode	7000 yr in an uncoupled mode	510 yr in a coupled mode

ECHAM3/LSG run, the two phases last, respectively, 15 000 and 7000 yr. On top of that, the ocean is further integrated for another 5000 yr with the same mean boundary conditions as before plus fluctuating fluxes, which are derived from an Atmospheric Model Intercomparison Project (AMIP) integration (Gates 1992) with the ECHAM3 model (Voss 1996). The GFDL spinup run is done by integrating the ocean-only model for 2400 yr. The sea surface temperature (SST) and salinity (SSS) are relaxed toward the observed values and the momentum flux is derived from the spin up of the atmospheric model. A technique (Bryan 1984) is used to accelerate the approach of the deep ocean toward its equilibrium state. The resulting effective length of time integration of the deep ocean is 34 000 yr (Manabe et al. 1991). Different from the two ECHAM/LSG runs and the GFDL run, the HadCM2 spinup run is performed in a coupled mode. Due to the high computational costs, the HadCM2 spinup run is at least one order of magnitude shorter than the other spinup runs. It starts from Levitus climatological values for potential temperature and salinity in the ocean interior and alternates between relaxation boundary conditions for SST and SSS and flux adjustments calibrated in the preceding relaxation phases (Johns et al. 1997). The coupled spinup run is designed to reduce the possible coupling shock. As will be seen in section 2b, the deep ocean of the HadCM2 model indeed does not have drifts that are as strong as those found in the ECHAM3/LSG run.

A long ocean-only spinup run allows the deep interior ocean to freely approach its own equilibrium state. However, what the minimum length of such a spinup run is and whether the final state will remain stable, that is, no drifting occurs when it is coupled to the atmosphere, are not known. It will be shown in section 2b that, despite a long spinup run, the state of ECHAM3/LSG ocean reveals a strong drift. For the HadCM2 run, in which an alternative coupled approach is used, the short integration time leaves little room for the deep ocean to freely approach its own equilibrium state. However, the use of Levitus climatological values as the initial conditions can cause the deep ocean to be close to its present-day state, since the circulation quickly adjusts the pressure field (which results from the given distribution of temperature and salinity). In any case, the quasi-equilibrium of the HadCM2 ocean is approached in a different manner as in the other three runs. This might be the cause that the pattern of the mean thermohaline circulation in the HadCM2 run differs from those in the other three runs (see section 2b).

b. Time-mean state, overall time evolutions, and total variances

This section considers the various mean thermohaline circulations, different trends, and spatial distributions of total variances in the four integrations. A few observed estimates of deep-ocean mass transport are given to provide the reader with some ideas about the quality of these first generation millennium integrations. The realism of the mean circulations is not the main concern here and will not be systematically studied.

Figures 1 and 2 show the Atlantic, Pacific, and the global streamfunctions in the four runs, averaged over 1000 yr. In the following, the circulations described by Figs. 1 and 2 are referred to as the time-mean circulation. The streamlines are plotted with the same interval for all runs so that the relative strength of the mass transport can be directly inferred.

The very gross features of the global overturning, that is, the deep-water formation in the North Atlantic, its subsequent southward spreading, and the upwelling in the Pacific and the Indian Ocean, are produced by all models. A deep anticlockwise overturning cell in the Southern Ocean is found in all runs (Fig. 2).

A closer inspection shows differences between the runs. The LSG model tends to produce a stronger overturning in the Atlantic and stronger upwelling in the Pacific than the GFDL and the HadCM2 models. A significant part of the overturning in the Atlantic does not leave this ocean, and the same is true for the Pacific; these parts therefore do not contribute to the global con-

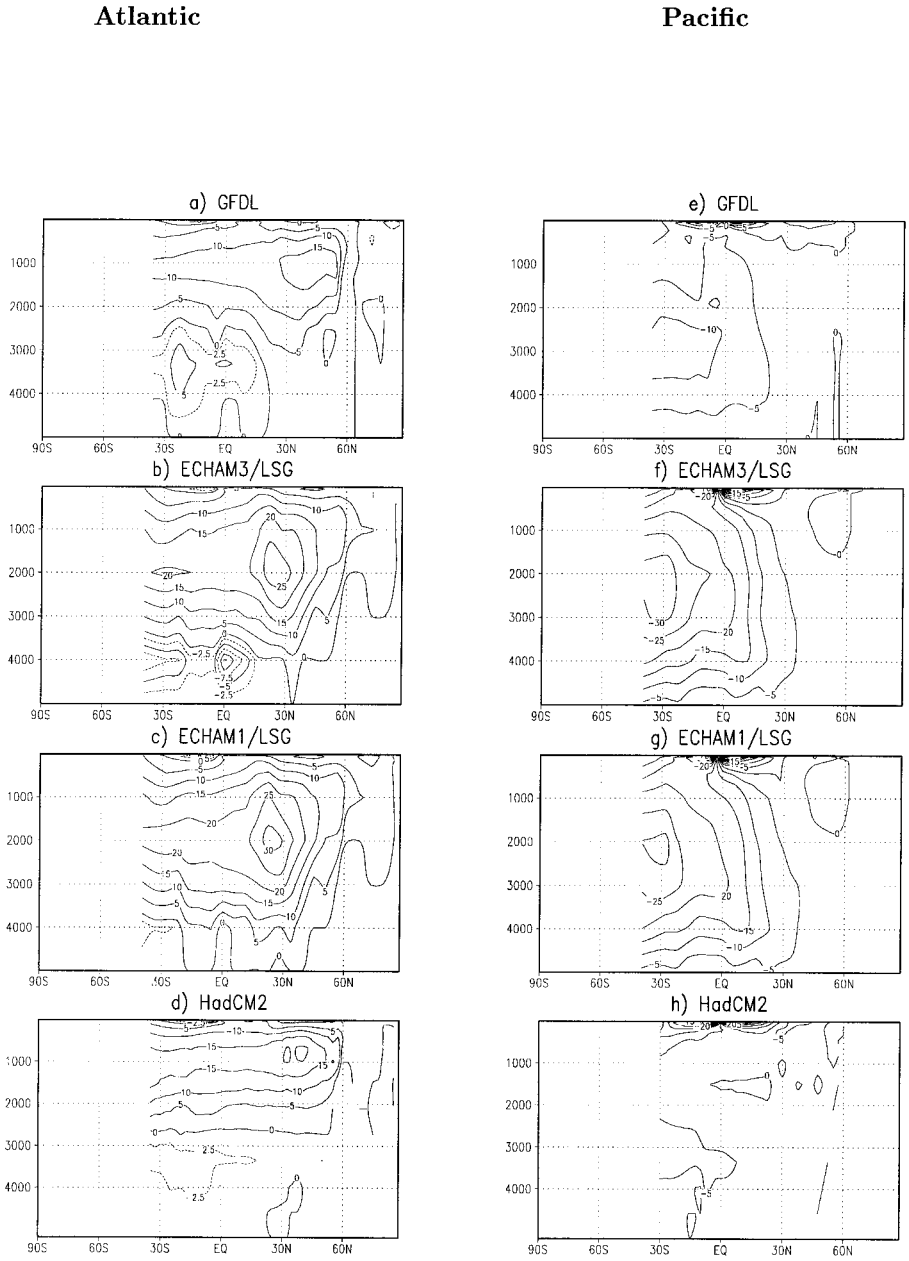

FIG. 1. The 1000-yr means of vertical–meridional sections of zonally averaged streamfunctions. Intervals of solid isolines are 5 Sv (Sv $\equiv$ 10^6 m^3 s^{-1}). For the negative streamfunctions in the Atlantic, additional isolines are plotted every 2.5 Sv.

veyor circulation. Moreover, the Atlantic overturning cell (described by the positive isolines) extends about 1000 m deeper and the downward branch of this cell is broader in the ECHAM/LSG runs than in the runs with the Bryan–Cox type of ocean model. Different from the Bryan–Cox type of ocean model, about half of the upwelled water in the Pacific joins the Ekman cell near the surface in the ECHAM/LSG runs.

Although the same type of ocean model is used in the GFDL and Had2CM runs, similar circulation patterns are only found in the upper 2000–2500 m of the Atlantic. In the deep Atlantic (below 3000–3500 m) and particularly in the Pacific, the HadCM2 circulation differs not only from those of the ECHAM/LSG runs, but also from that of the GFDL run. It is much more sluggish than the circulations in the other runs. In the Pacific, the circulation cell with the upwelling in the tropical regions is hardly noticeable in the HadCM2 run. This situation is further demonstrated by the global streamfunction in Fig. 2. While the circulations in the GFDL and the two ECHAM/LSG runs reveal a two-cell structure in the meridional direction (though with different

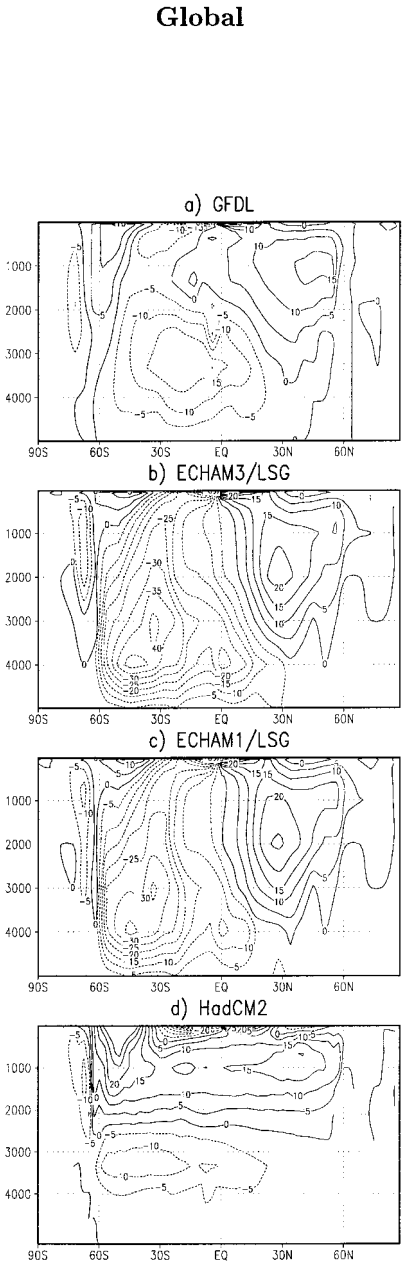

FIG. 2. The 1000-yr means of vertical–meridional sections of zonally averaged global streamfunctions. Intervals of solid isolines are 5 Sv.

strengths), the HadCM2 run shows a two-cell structure in the vertical direction. Because of the sluggish Pacific circulation (Fig. 1h), the overturning cell in the intermediate depth of the Atlantic dominates the pattern of the global circulation in Fig. 2d.

The mean circulations are also quantified by time series of the maximal overturning (Fig. 3). Overall, the overturning is stronger in the two ECHAM/LSG models than in the GFDL and the HadCM2 models. The weak transports in the deep Pacific and deep Indian Ocean of the HadCM2 run are documented by the small magnitudes of streamfunctions (the uppermost line in Figs. 3b and 3c). The Atlantic overturning circulation in the ECHAM3/LSG run is much weaker than that in the ECHAM1/LSG run. The Atlantic overturning flow is about 18 Sverdrups (Sv $\equiv 10^6$ m^3 s^{-1}) in the GFDL run, about 21 Sv in the HadCM2 model, about 31 Sv in the ECHAM3/LSG run, and about 36 Sv in the ECHAM1/LSG run. In the Pacific and the Indian Ocean, it reaches about 13 for both oceans in the GFDL run, 35 and 20, respectively, in the ECHAM3/LSG run, 32 and 24 in the ECHAM1/LSG run, and 9 and 1.5 in the HadCM2 model. It is noted that Fig. 3 describes only the strength of the circulation under the assumption of a meridional circulation. In the case of the Pacific in the HadCM2 run, in which a meridional circulation is not fully developed, the time series is not representative for maximum overturning. In fact, the HadCM2 time series in Fig. 3b corresponds only to values of the streamfunction in a very small region.

Using observational data in the Atlantic, Roemmich and Wunsch (1985) estimated that 17 $\pm$ 4 Sv of relatively warm thermocline and intermediate water flow northward at 24°N; and below this 20 $\pm$ 5 Sv, identified as North Atlantic Deep Water (NADW), flow southward. Further below, about 3 $\pm$ 3 Sv of Antarctic Bottom Water (AABW) flow northward. Figures 3 and 1 suggest that the transport of the NADW in the GFDL and the HadCM2 runs is close to the lower bound of the estimates of Roemmich and Wunsch and that in the two ECHAM/LSG runs it is close to or above the upper bound of these estimates. The northward transport of AABW is underestimated in the ECHAM1/LSG. The numbers produced by the ECHAM3/LSG run are more comparable to the values of Roemmich and Wunsch than those produced by the ECHAM1/LSG run.

Observations of the transport at 24°N in the Pacific (Bryden et al. 1991), though highly uncertain, show 8 Sv of southward transport of deep water and 5 Sv of northward bottom transport. In Figs. 1e–h at 24°N, the circulation shows prevailing upwelling in the GFDL and the ECHAM/LSG runs and is very sluggish in the HadCM2 run.

The distributions of standard deviations of the zonally averaged streamfunctions are shown in Fig. 4. All coupled models produce similar gross distributions of variances, in spite of the differences in the time-mean circulations. In the Atlantic and the Pacific, the models produce, or tend to produce, two maxima of standard deviation located in the subtropics at intermediate depth. A closer inspection shows that the maximum in the North Atlantic extends to a deeper layer in the GFDL and the ECHAM/LSG runs than in the HadCM2 run. This result indicates that the variability of the deep North Atlantic is weaker in the HadCM2 run than in the other three integrations. Another difference between the four runs concerns the amplitudes of standard deviation. The smallest values are found in the ECHAM1/

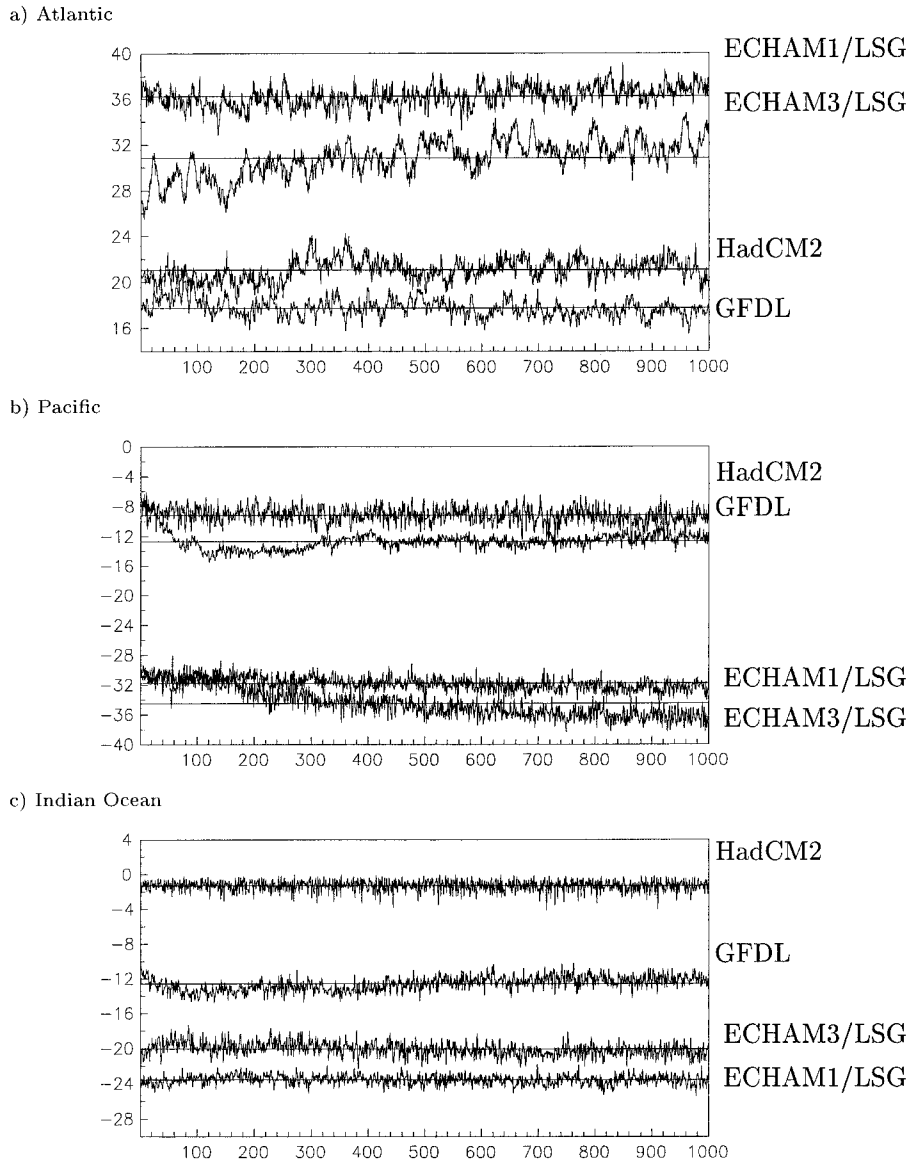

FIG. 3. Time series of maximal overturning (Sv). The maximal overturning is defined as the maximum of the positive streamfunction in the Atlantic and as the minimum of the negative streamfunction below 1000 m in the Pacific and the Indian Ocean. The horizontal lines indicate the 1000-yr averages.

LSG run in both oceans. In the Pacific, the largest standard deviations are found in the HadCM2 run. The small maximum at 4000-m depth in the Atlantic in the HadCM2 run (Fig. 4d) is induced by a jump of 2–3 Sv within a few decades (see Figs. 5 and 8d).

Figure 3 shows that, for all four runs, the total variance, as described by the standard deviation in Fig. 4, consists of a large amount of interannual to interdecadal variability in the Atlantic, whereas the total variances in the Pacific and the Indian Ocean contain variability on shorter timescales. A more detailed analysis of frequency-decomposed variances is given in section 3. An analysis of the 50–70-yr oscillation of the North Atlantic overturning, which is evident in Fig. 3a, is given by Delworth et al. (1993).

Besides the discrepancies in the mean and the variability, different types of drifts are found. Concerning the strength of the thermohaline circulation in the Pacific and the Indian Ocean, Figs. 3b and 3c, the GFDL run reveals an increase in the first 100 yr and a gradual decrease during the following centuries. An initial drift during the first 200 yr was also evident in the 1260-yr integration with the ECHAM1/LSG model (von Storch et al. 1997). The last 1000 yr of this integration reveals a small, nearly linear drift, which is most apparent for the Pacific time series in Fig. 3b. The ECHAM3/LSG

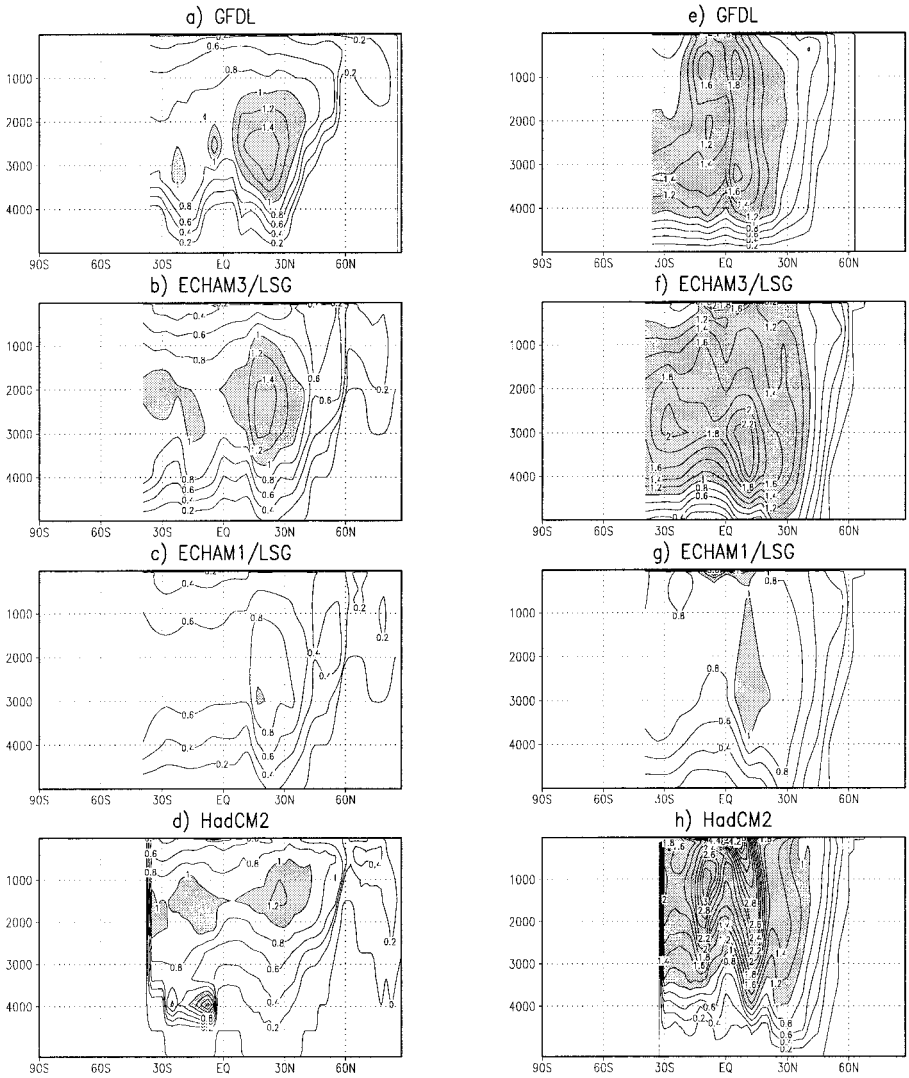

FIG. 4. Std devs of the interannual zonally averaged streamfunctions in each basin. The interval between the isolines is 0.2 Sv in all diagrams. Areas with standard deviations larger than 1 Sv are shaded.

run shows a strong linear trend in the strength of the overturning circulation in the Atlantic and the Pacific over almost the entire integration period. In the Atlantic, the maximum streamfunction increases from about 28 Sv at the beginning of the integration to about 33 Sv after 1000 yr. For the HadCM2 run, a ''jump'' or a ''shift'' in year 260 (Tett et al. 1997) is found for the maximal overturning in the Atlantic (Fig. 3a).

The jump is shown more clearly in Fig. 5. The top curve in Fig. 5 is identical to the HadCM2 time series in Fig. 3a, but for the entire 1592 yr. This rapid change is related to changes in convection south of Greenland and may have a similar nature to the decadal variations described by Rahmstorf (1995). The two lower curves show the streamfunction at two grid points. Besides the jump in the time series of the maximal overturning, which represents the streamfunction at about 1000-m depth, there is another jump in the time series at about 4000-m depth (the bottom time series in Fig. 5). Overall, the HadCM2 run reveals little linear drift, despite the relatively short spinup integration.

The drifts shown in Figs. 3 and 5 are not the only

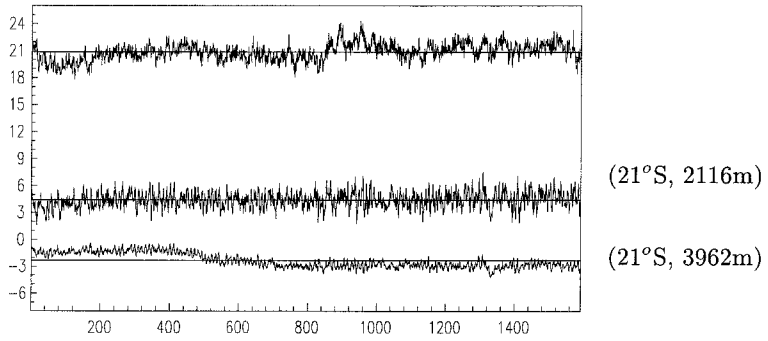

FIG. 5. HadCM2 time series of maximal overturning in the Atlantic and the streamfunction at 21° at 2116-m depth and at 3962-m depth. The horizontal lines indicate the 1592-yr averages. The label of time axis is different from that in Fig. 2. Year 593 in this diagram corresponds to year 1 in Fig. 2.

types of drifts generated by the coupled models. The presence of drifts significantly influences the spectral features at low frequencies. In this paper, drifts are considered as artifacts of the models, rather than as a part of the variability to be studied. Since many drifts do not appear as linear trends, they cannot easily be removed. In the following analysis, the trends in the GFDL and the HadCM2 models are not removed, but are taken into account in the interpretation of the results. For the two ECHAM/LSG runs, whose trends are essentially linear, least squares fitted linear trends are subtracted from the data prior to the analysis.

3. Spectral properties

A spectral power law describes a scale-invariant relation over a broad range of frequencies. If a power law holds, no spectral peaks can be identified. There exists a frequency range $\Delta\omega$ such that the considered spectrum $\Gamma(\omega)$ can be described by

$$\Gamma(\omega) = \alpha\omega^{-\beta} \quad \text{for } \omega \in \Delta\omega, \tag{1}$$

where α and β are constants. A spectrum described by (1) has a linear slope for $\omega \in \Delta\omega$ in a log–log plot. Here $\beta > 0$ represents a slope where the spectral level increases with decreasing frequency.

In section 3a, the spectral slope β is estimated by least squares fitting (1) to spectra over two frequency ranges. One covers high frequencies from the highest resolvable frequency down to $\omega_o = 1$ cycle $(20\ \text{yr})^{-1}$, and the other covers low frequencies from the lowest resolvable frequency up to ω_o. These two frequency ranges are denoted by $\Delta\omega_h$ and $\Delta\omega_l$ and the corresponding slopes by β_h and β_l, respectively. Although the consideration of a low- and a high-frequency range is motivated by the expectation of different power laws over high- and low-frequency ranges, the choice of ω_o is quite arbitrary. The values of β obtained by fitting (1) into spectra must be interpreted with care. In the following analysis, the distributions of β_h and β_l serve only as a rough estimation of the general tendency of the slopes. Separate spectral analyses are carried out to verify the values of β.

Spectral power laws are often used to diagnose the underlying dynamics of the system. For instance, the result of β_l provides information about the maximal memory timescale of the considered variable. It is known that, if the autocorrelation function of a variable goes to zero sufficiently fast for time lag τ larger than τ^*, the spectrum $\Gamma(\omega)$ will be flat for frequencies ω smaller than $\omega^* = 1/\tau^*$. White noise represents the extreme situation in which $\tau^* = 0$. In this case, the autocovariance function is zero for $\tau > \tau^* = 0$ and the spectrum is white for $\omega < 1/\tau^* = \infty$, that is, for all ω. On the other hand, a variable whose lag-correlation function tends to zero for $\omega > \tau^*$ can be interpreted as a variable of a system that has a finite memory. The whiteness of a spectrum at low frequencies can therefore be used as a measure of the maximal memory timescale of the system. If β_l is notably larger than zero, that is, the low-frequency part of the spectrum is not white, the maximal memory timescale will be longer than the longest resolvable timescale of the considered time series.

It is noted that the memory timescale defined above and the age of a water mass describe different aspects of the ocean. The former is a property of fluctuations related to covariance function or spectrum, whereas the latter indicates the time since the water enters the deep layers. An old water mass can vary on different timescales and have a memory timescale different from the age of the water mass.

For variables describing baroclinic Rossby waves in the ocean, the spectra level off at a frequency ω^* of about one cycle every few decades and become flat for frequencies ω smaller than ω^* (Frankignoul et al. 1997), suggesting that the maximal memory of these waves is no longer than a few decades. The timescale of about a few decades is comparable to the time for a long baroclinic Rossby wave to cross an ocean basin. For the atmosphere, an estimation using the coupled ECHAM1/LSG model suggested that the atmospheric timescale $1/\omega^*$ is of the order of one year for variables not strongly affected by tropical SST anomalies (von Storch 1994, 1999). The analysis in section 3a leads to the deter-

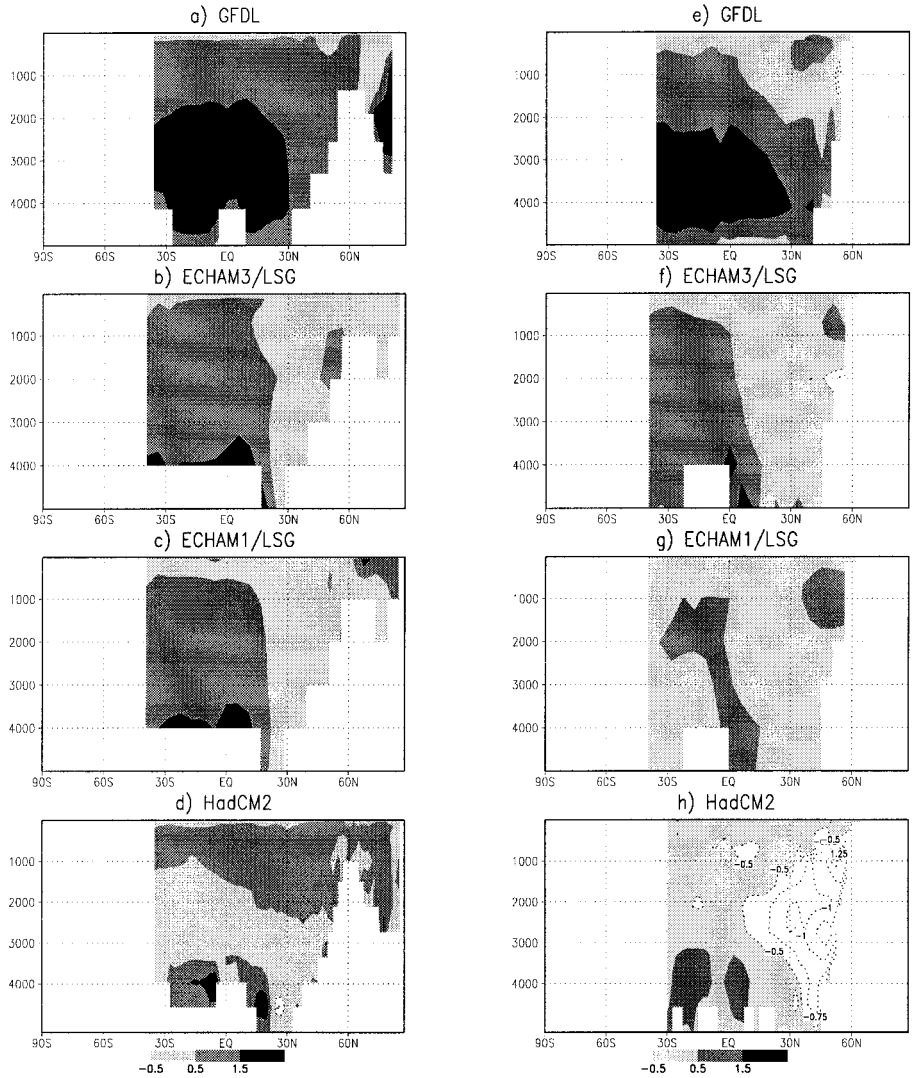

FIG. 6. Low-frequency spectral slope β_l of zonally averaged streamfunctions in the Atlantic and Pacific. The black, dark, and light gray areas indicate the areas where values of the spectral slope β_l are close to two, one, and zero, respectively. White areas with dashed lines indicate areas with $\beta_l < -0.5$.

mination of the maximal memory timescale, $1/\omega^*$, for the transport of different deep-water masses.

a. Spectral power laws for the transport of different water masses

In this section, spectra for the transport of different water masses are studied using gridpoint time series of zonally averaged streamfunctions. Two consecutive chunks are used to estimate the spectra. For a yearly time series of 1000-yr length, the smallest resolvable frequency is then one cycle per 500 yr. Equation (1) is fitted to the low- and high-frequency parts of these spectra. Distributions of β_l and β_h for the Atlantic and the Pacific are shown in Figs. 6 and 7. In general, the spectral level in the shaded areas remains essentially constant or increases with decreasing frequencies, and the spectral level in the white areas with dashed lines decreases with decreasing frequencies.

The distributions of low-frequency slope β_l (Fig. 6)

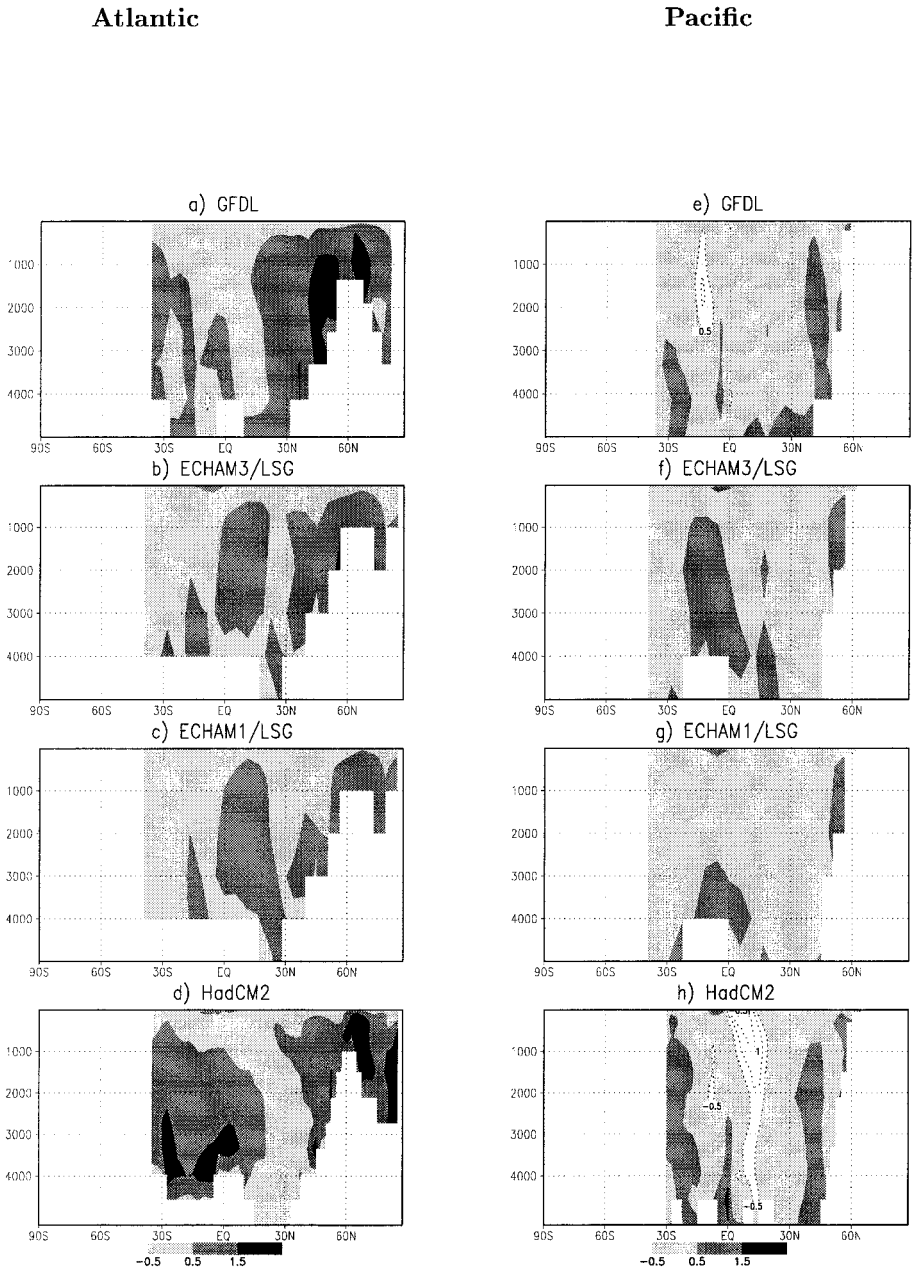

FIG. 7. Same as Fig. 6 but for high-frequency spectral slope β_h.

can be classified into two groups. The first one consists of the Atlantic sections of the GFDL and two ECHAM/LSG runs (Figs. 6a–c) and the sections of the GFDL and the ECHAM3/LSG runs in the Pacific (Figs. 6e and 6f). These sections are characterized by the increase of β_l with increasing depth in the tropical and the subtropical oceans, with β_l being zero near the surface and close to one in the intermediate depth and close to two near or at the bottom. The regions with $\beta_l \sim 2$ in the GFDL and ECHAM3/LSG runs extend to about 60°S in the sections of global streamfunctions (not shown). In the southern ocean (not shown) and in the North Atlantic and North Pacific, β_l varies little with depth and has values close to zero.

For the second group, which consists of the Atlantic section of the HadCM2 run (Fig. 6d) and the Pacific sections of the ECHAM1/LSG and HadCM2 runs (Figs. 6g and 6h), the distributions of β_l deviate notably from those described above. The main difference concerns β_l in the intermediate and deep oceans. Apart from a few spots in the HadCM2 run, the spectral slopes in the intermediate and deep Atlantic and Pacific are close to zero, as indicated by large areas with light gray in Figs. 6d, 6g, and 6h. Here β_l is also close to zero in the

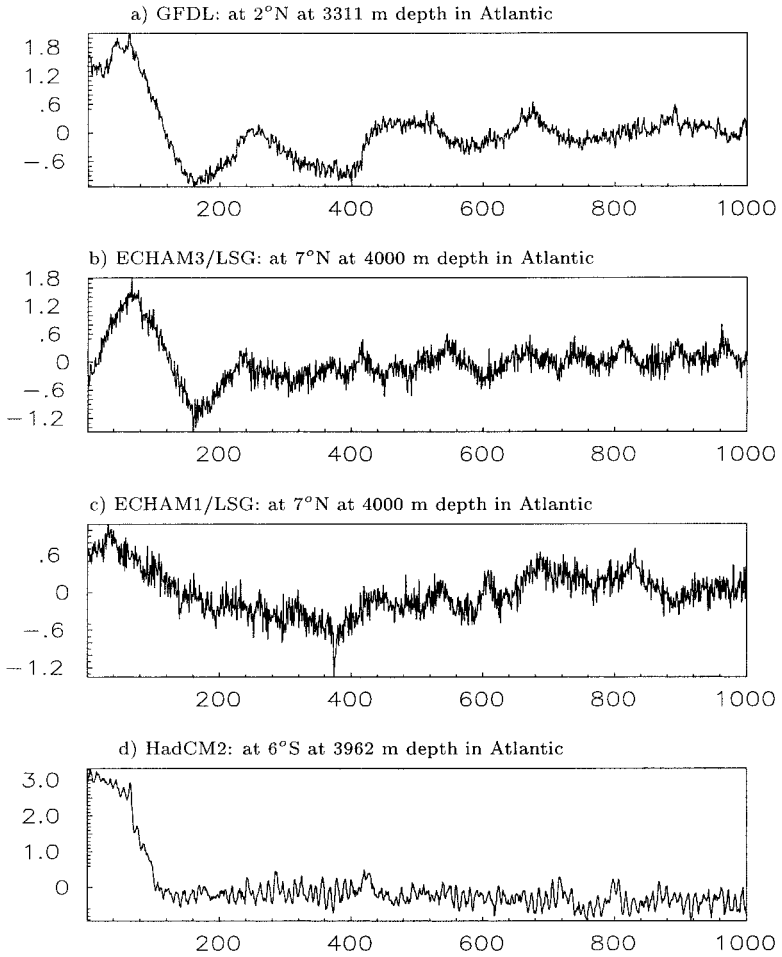

FIG. 8. Time series at Atlantic grid points at which $\beta_l \sim 2$. The locations are noted above each curve.

Southern Ocean (not shown). In the North Pacific of the HadCM2 run, there is even a large area where β_l is smaller than zero, indicating that the spectral level decreases with decreasing frequency at low frequencies. In general, the increase of spectral energy with decreasing frequency is not present or strongly reduced in the second group of integrations. The black spot in the deep Atlantic of the HadCM2 run is related to a jump occurring during the integrations (see Figs. 5 and 8d).

A comparison between Figs. 6 and 1 suggests that the strength of low-frequency variations, as characterized by β_l, is related to the time-mean circulation. The weakest low-frequency variations (characterized by $\beta_l \sim 0$ or $\beta_l < 0$) are found in the HadCM2 run, in which the Pacific circulation cell with upwelling in the tropical regions is essentially absent, resulting in a different global circulation pattern in Fig. 2d. The differences found in the Pacific of the ECHAM3/LSG and ECHAM1/LSG integrations (Figs. 6f,6g) may be related to the different spinup runs.

The distribution of β_l can be used to characterize the maximum memory timescale of different water masses. For the GFDL, the ECHAM3/LSG, and partly for the ECHAM1/LSG runs, the result that the spectral level of zonally averaged streamfunctions increases with decreasing frequency at low frequencies in the deep tropical and subtropical oceans suggests that the maximal memory timescale there is longer than a few centuries. The situation changes in the mid- and highlatitude regions, where the low-frequency slope β_l is close to zero, indicating a maximal memory timescale of about a few decades. To obtain the maximal memory timescales of deep tropical and subtropical oceans and to characterize the related variations up to this timescale, integrations over time periods longer than 1000 yr are required.

Figure 7 shows the distributions of the high-frequency spectral slopes β_h in the Atlantic and the Pacific. The differences among the runs are not as large as for the low-frequency slope β_l. For all models, β_h values are slightly larger than zero in the northern North Atlantic, about 1 to 2 in the Southern Ocean (not shown) where an anticlockwise overturning cell is found in Fig. 2, and are around zero or smaller than zero in the Pacific and the Indian Ocean. In the GFDL and two ECHAM/LSG

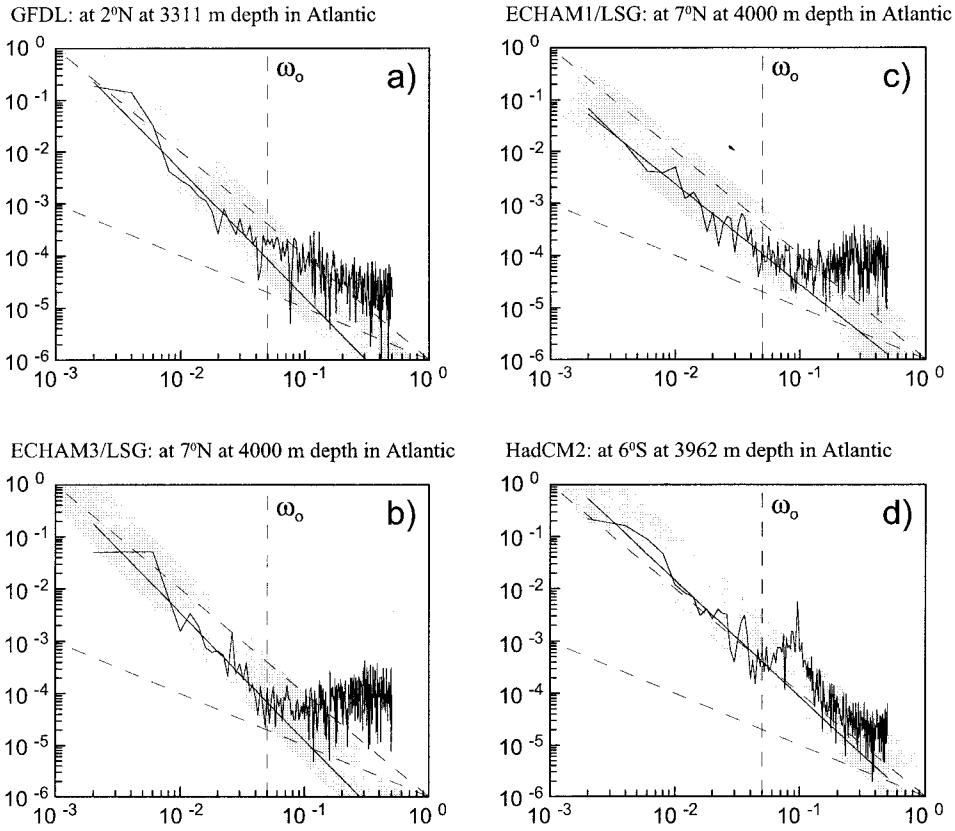

FIG. 9. Spectra of the time series at grid points in the Atlantic where $\beta_l \sim 2$. The locations are noted above each curve. The spectra are estimated from two consecutive chunks. Such obtained spectral values are χ^2 distributed with four degrees of freedom for all frequencies (except for the highest and the lowest resolvable frequencies $\omega = 0.5$ and $\omega = 2 \times 10^{-3}$). The gray band shows the 95% confidence band of the χ^2 distribution. The solid straight line is obtained by least squares fitting Eq. (1) to the low-frequency part of the spectrum (i.e., for $\omega \in \Delta\omega_l$). Here ω_o, which divides the low-frequency band $\Delta\omega_l$ from the high-frequency band $\Delta\omega_h$, is marked by the vertical dashed line. The two other dashed lines are proportional to ω^{-1} and ω^{-2}.

models, the high-frequency slope β_h becomes smaller in the tropical and subtropical Atlantic. In the HadCM2 model, the β_h values reveal another maximum in the subtropical Atlantic, which is partly produced by the strong oscillation on timescales of about 10 yr in that region (see section 3b).

The sensitivity of the fits was tested by redoing the analysis with the first 200 yr of the data removed. Similar results are also obtained when the linear trends in the remaining time series are removed. The resulting distributions of β_l and β_h were similar to Figs. 6 and 7.

b. Verifications of the spectral power laws

To verify the power laws found in section 3a, time series and spectra at some representative grid points are considered. It will be shown that (1) is an appropriate approximation for the spectra.

Figures 8 and 9 show time series and their spectra at grid points in the Atlantic where $\beta_l \sim 2$. In Fig. 9, the fitted spectral slope and the 95% confidence band are indicated. The confidence band characterizes the variations of the chunk spectral estimator. If the fitted spectral slope represents the true spectrum, 95% of the estimated spectral values should lie within the confidence band. The two dashed lines are proportional to ω^{-2} and ω^{-1}, respectively.

All the grid points considered in Figs. 8 and 9 are located in the tropical oceans at 3000–4000-m depth. The low-frequency parts of the spectra at these grid points (Fig. 9) reveal a slope close to ω^{-2}. Almost all spectral values with $\omega \in \Delta\omega_l$ lie within the 95% confidence band. No preferred timescale exists in the considered frequency range $\Delta\omega_l$. Outside $\Delta\omega_l$, a significant peak near one cycle per 10 yr is found for the time series of the HadCM2 model (Fig. 9d). The overall result suggests that the considered time series can be approximately described by the power law of ω^{-2} for $\omega \in \Delta\omega_l$.

Concentrating only on the low-frequency variations, Fig. 8 indicates that the time series of the HadCM2 model (Fig. 8d) behaves differently to those of the GFDL and two ECHAM/LSG models (Figs. 8a–c). The former reveals, apart from the jump, pronounced variations on essentially one timescale, namely the timescale of about 10 yr (see also the spectral peak shown in Fig. 9d). In contrast to that, the first three time series in Fig.

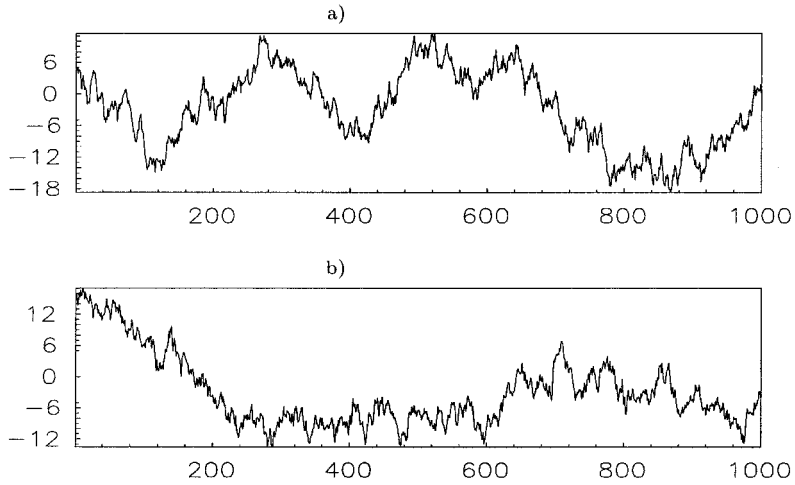

FIG. 10. Two pieces of an AR(1) time series. The parameter of the process is 0.99.

8 reveal rich structures of variations on many long timescales. Consistent with this observation, the low-frequency spectral slope estimated from the last 880 yr of the HadCM2 time series (i.e., when the jump is excluded from the analysis) is smaller than two. For the GFDL and the ECHAM3/LSG time series, which reveal large initial oscillations, the distribution of β_l derived from the last 800 yr is almost unchanged compared with Fig. 6. Thus, the spectral features of the GFDL and ECHAM3/LSG time series have little to do with the initial oscillations. This result suggests that the ω^{-2} power law is a more robust feature of the time series of the GFDL and two ECHAM/LSG models than of the time series of the HadCM2 model.

When focusing only on low-frequency fluctuations, one notices that the most pronounced fluctuations in Fig. 8 visually differ from each other. It is suggested that such a difference results from the use of not long enough time series to study the long memory process in the deep ocean. Such a possibility is verified by considering a first-order autoregressive [AR(1)] process, which produces a ω^{-2} power law at low frequencies. To ensure that the time series generated by the process has a ω^{-2} spectral shape at the frequencies of interest, a large process parameter of 0.99 is chosen. A time series with a length of 10 000 is produced by such an AR(1) process. Two pieces of this time series with length of 1000 are shown in Fig. 10. The corresponding spectra, estimated and plotted in the same manner as in Fig. 9, are shown in Fig. 11.

Unlike the time series shown in Fig. 8, which reveal different levels of high-frequency variation, the two time series shown in Fig. 10 have the same levels of high-frequency variation. However, when concentrating only on the low-frequency variations, the difference between the two time series in Fig. 10 appears to be comparable with the differences seen in Figs. 8a–c. As observed in Fig. 8, the one time series tends to oscillate on one timescale and the other time series tends to undergo a long-term fluctuation. As in Fig. 9, the spectral slopes are close to ω^{-2}. This result suggests that due to the shortness of the time series, the different low-frequency variations found in time series of the GFDL and two ECHAM/LSG models cannot be considered to be generated by distinctly different processes.

Figure 10 also demonstrates that the appearance of

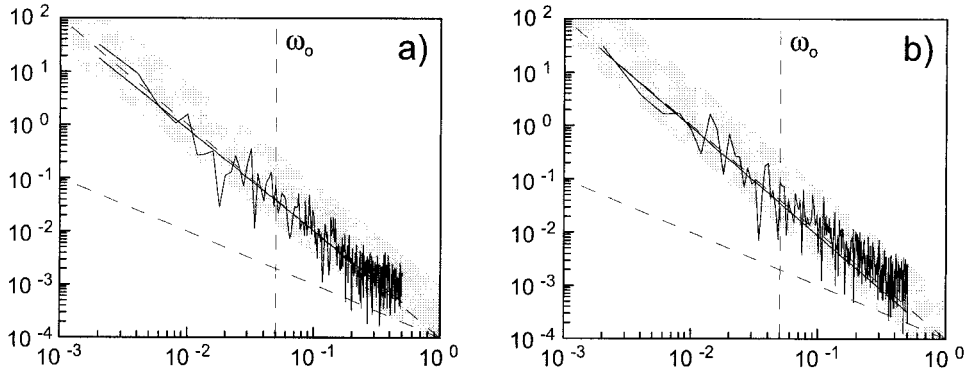

FIG. 11. Spectra of the time series shown in Fig. 10, estimated and plotted in the same manner as in Fig. 9.

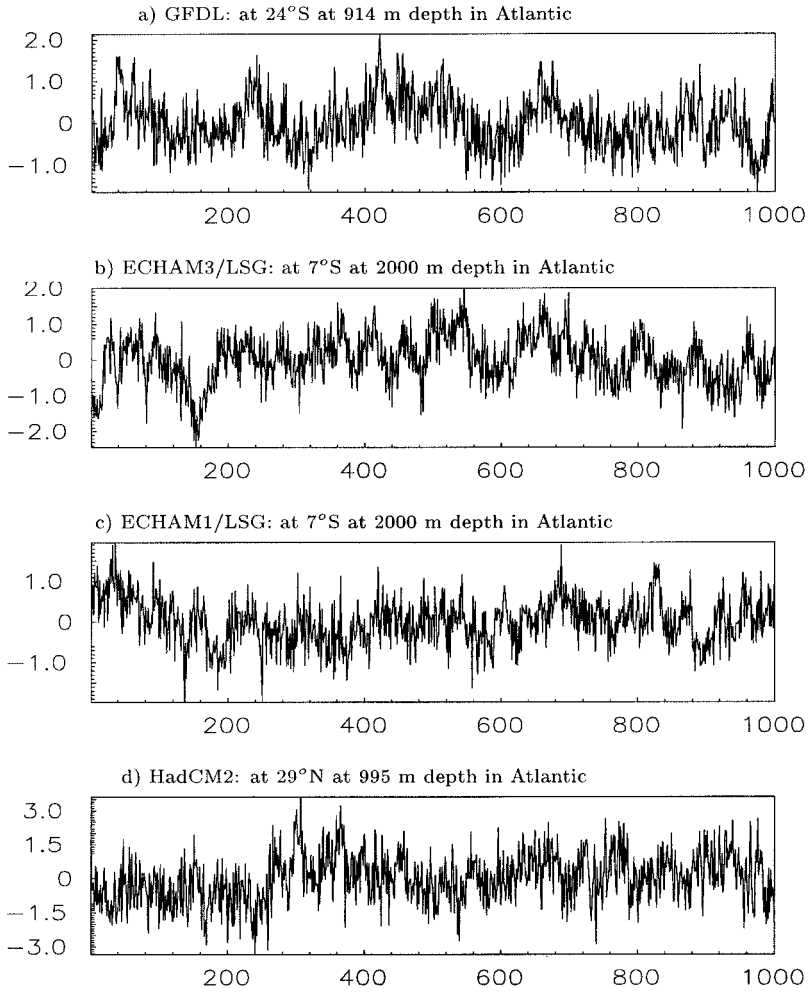

FIG. 12. Time series at grid points in the Atlantic at which $\beta_l \sim 1$. The locations are noted above each curve.

periodicities in the time series does not necessarily imply a spectrum with peaks. The fact that the spectra of mass transport can be approximated by Eq. (1) suggests that these spectra are continuous and do not have isolated maxima.

Figures 12 and 13 show time series and their spectra at grid points in the Atlantic where $\beta_l \sim 1$. These grid points are located at intermediate depth. All spectra shown in Fig. 13 reveal a low-frequency power law $\omega^{-\beta_l}$, with β_l being close to one. As in Fig. 8, different low-frequency variations are involved in different runs. In particular, the time series of the GFDL model (Fig. 12a) reveals variations on a timescale of about 200 yr, and that of the ECHAM3/LSG model (Fig. 12c) shows variations on a timescale of about several decades. These variations, however, produce no significant spectral peaks. As in the case of the ω^{-2} power law, time series with $\beta_l \sim 1$ should have notable low-frequency variations. Because of the shortness of the time series, these variations may look different to each other, even when they are produced by exactly the same process.

Figures 14 and 15 shows time series and their spectra for grid points in the northern North Atlantic where the high-frequency slope β_h is larger than zero. The time series behave significantly differently to those for the tropical and subtropical Atlantic. The spectral slope over the high-frequency range is between one and two.

The time series in the region where $\beta_l < 0$ in the North Pacific of the HadCM2 run (Fig. 6h) are also considered. The spectra (not shown) are essentially flat at high frequencies for ω larger than one cycle per a couple of decades and decrease with decreasing frequency at the rate of about ω at lower frequencies.

To summarize, the spectra of zonally averaged streamfunctions can be reasonably well represented by the power laws obtained from least-squares fit. Except for the HadCM2 run, the spectral features are essentially scale invariant for both $\omega \in \Delta\omega_l$ and $\omega \in \Delta\omega_h$ and do not reveal significant peaks in the considered frequency ranges. Here β_l increases in the tropical and subtropical oceans from about zero near the surface to about one at intermediate depth (represented by the grid points

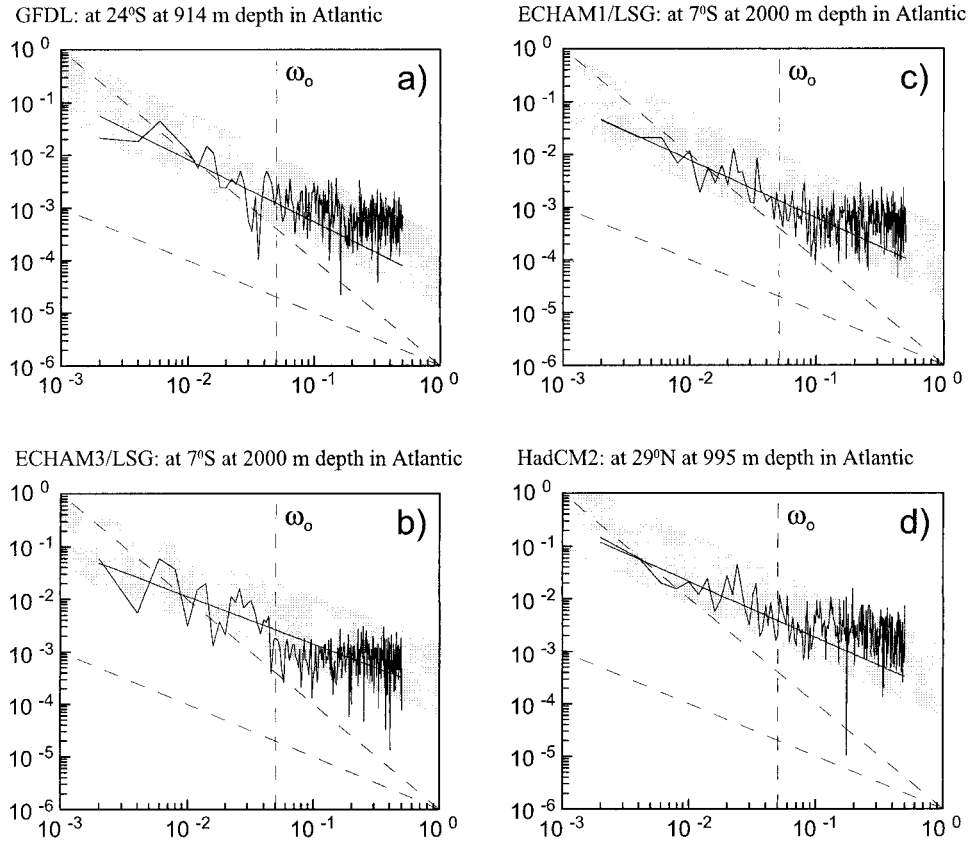

FIG. 13. Spectra of the time series at grid points in the Atlantic at which $\beta_l \sim 1$; the spectra are estimated and plotted in the same manner as in Fig. 9. The locations are noted above each curve.

considered in Figs. 12 and 13) and to about two further below (represented by the grid points considered in Figs. 8 and 9). In the northern North Atlantic (represented by the grid points considered in Figs. 14 and 15) and in the Southern Ocean, β_l tends to be close to zero, but β_h is notably larger than zero. The large values of the low-frequency slope β_l found for deep water masses in the GFDL and ECHAM3/LSG runs are not significantly affected by strong initial oscillations. The different low-frequency variations in regions with $\beta_l \sim 1$ and $\beta_l \sim 2$ do not necessarily indicate different types of low-frequency variations. They may result from the fact that time series used to study long-memory processes are too short.

4. The dominant spatial characteristics

The dominant spatial characteristics are studied using EOF analysis. The analyses are carried out for vertically weighted anomalies. The weighting is necessary, because deep water masses behave differently from water masses in the upper layer, as indicated in section 3, and the upper ocean (say in the upper 1000 m) is represented in all models by more layers than the deep ocean. Figure 16 shows the first EOFs of zonally averaged streamfunctions in the Atlantic and the Pacific for the four integrations. The two leading EOFs taken together explain one-half to two-thirds of the total variances of the streamfunctions in each integration.

Apart from some small-scale details, the two leading EOFs in all four runs reveal a similar large-scale structure. Unlike the time-mean circulation, which is characterized by open isolines, the first leading EOFs (Fig. 16) are described by essentially closed isolines. The tendency for the isolines to be closed is more apparent in the Atlantic for all runs and in the Pacific for the two ECHAM/LSG runs. The closed isolines indicate recirculations within each ocean basin. This result suggests that the spatial scale of the most dominant large-scale variations is smaller than that of the time-mean circulation. The locations of the patterns suggest that the recirculations involve water masses at intermediate depth. Consistent with this, the low-frequency spectral slope β_l of the corresponding principle components (not shown) has values similar to those found at intermediate depth in Fig. 6. In the Atlantic, the center of the recirculation is located farther south and down relative to the maximum of the streamfunctions in the time-mean sections (first column in Fig. 1). In the HadCM2 run, it is even shifted south of the equator. Since the locations

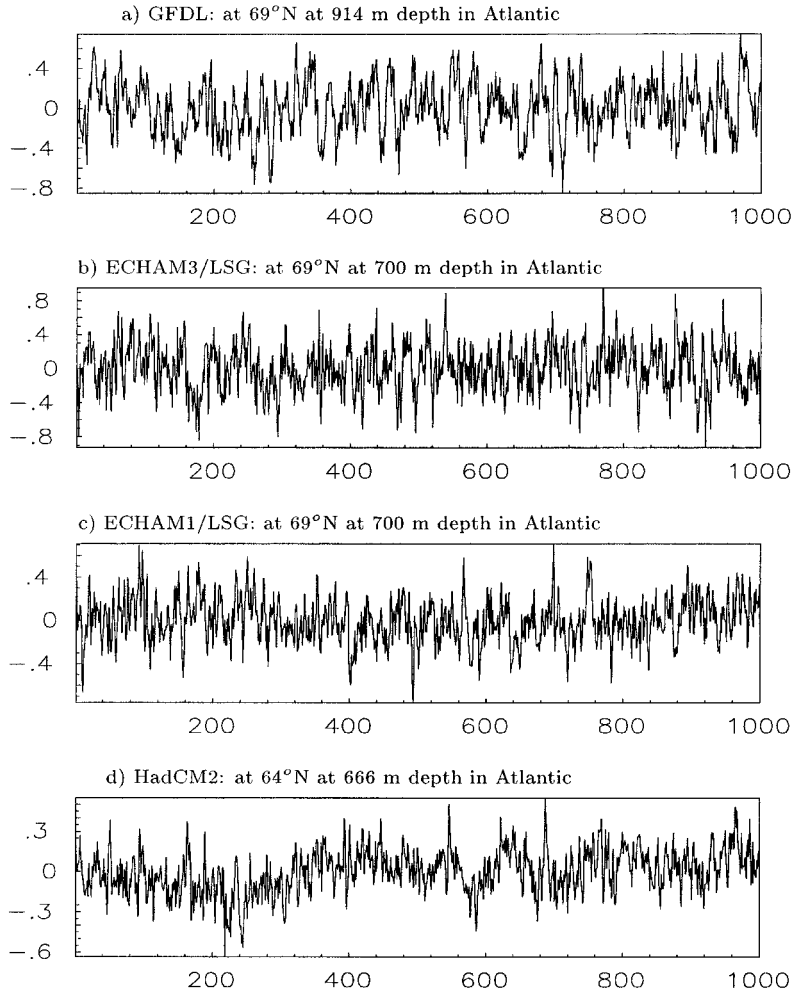

FIG. 14. Time series at Atlantic grid points at which $\beta_h > 0$. The locations are noted above each curve.

of the maximum of the time-mean overturning deviate from the locations of the center of the recirculations, the first EOFs do not describe the fluctuations in the strength of the overturning.

The major difference between the leading Atlantic EOF in the four runs (the first column of Fig. 16) is due to the shape of the anomalous recirculation. Relative to the HadCM2 integration in Fig. 16d, the anomalous recirculation extends to deeper layers in the GFDL and two ECHAM/LSG integrations (Figs. 16a–c).

In the Pacific, the leading EOFs in the GFDL and HadCM2 models tend to have two local centers just off the equator, whereas EOF1 in the two ECHAM/LSG models show one large center north of the equator. A comparison with the mean circulation (second column in Fig. 1) shows that the recirculation centers north of the equator in the GFDL and two ECHAM/LSG runs coincide with the region of the upwelling from the deep North Pacific. Such a correspondence between the mean flow and the leading EOF is not apparent for the HadCM2 model.

The second leading EOFs (not shown) show dipole structures and describe, therefore, variations with smaller meridional scales. Apart from some details, the large-scale features of the EOF2 of the four runs are comparable to each other. They describe anomalous circulations of the intermediate water masses.

The streamlines shown by the leading EOF suggest that anomalous large-scale motions tend to be confined to each ocean basin. The connection between recirculations in two different ocean basins is quantified by the simultaneous correlations listed in Table 2 between the first two leading Atlantic PCs and the first two PCs in the Pacific and the Indian Ocean for the four integrations. For different runs, the lagged correlations between the PCs (not shown) are within the same ranges as those shown in Table 2.

For a time series whose maximal memory timescale is too long to be properly detected from the available time series, the equivalent sample size is extremely small. Since the significance of the correlations crucially depends on the equivalent sample size (Zwiers and

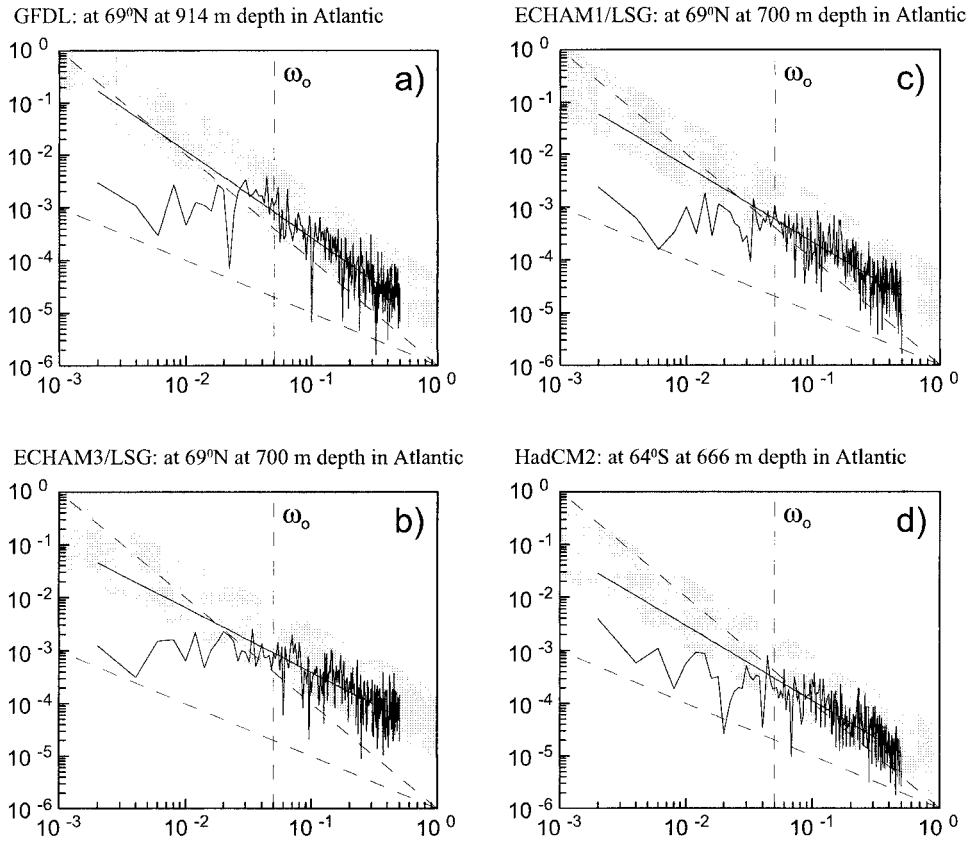

FIG. 15. Spectra of the time series at Atlantic grid points at which $\beta_h > 0$; spectra are estimated and plotted in the same manner as in Fig. 9. The locations are noted above each curve.

Storch 1995), it becomes extremely difficult to assess the significance of the correlations. The estimation of equivalent sample size is beyond the scope of this paper. To have some feeling about the effect of this parameter on the correlations shown in Table 2, two examples are considered. If the equivalent sample size is 10, correlations larger than 0.55 are significantly different from zero. If the equivalent sample size is 50, correlations larger than 0.24 are significantly different from zero. The maximal memory timescale of the leading EOF is about a few centuries or longer in the GFDL and ECHAM3/LSG runs and partly in the ECHAM1/LSG run. For these integrations, the significance level is expected to be larger than 0.55. For the HadCM2 run, the smaller memory timescale implies a much lower significance level. Following this consideration, Table 2 indicates that the connection between the dominant large-scale modes in the Atlantic and in the other oceans is likely not statistically significant.

5. Conclusions

This paper estimates the statistics of deep-ocean mass transport from four 1000-yr integrations with coupled atmosphere–ocean GCMs. Two aspects of deep ocean variations are considered. One concerns the spectral power laws and the other the dominant spatial characteristics. Because of the lack of observations and the limitation of ocean-only GCMs, these are still unknown and have to be studied using fully coupled GCMs.

By considering the least squares fitted spectral power laws, the spectral features of mass transport are identified and classified. When considering the low- and high-frequency ranges separately, the overall spectral features can be described by frequency-invariant power laws of the type of $\omega^{-\beta}$. For the deep tropical and subtropical ocean, the distributions of slope β_l of low-frequency spectra vary from integration to integration and depend crucially on the time-mean state of the ocean. Here β_l is notably larger than zero (i.e., $\beta_l \sim 1$ to 2) in the GFDL and ECHAM3/LSG runs and partly in the ECHAM1/LSG integration but close to zero in the HadCM2 integration. The result suggests that low-frequency variations are more intense in the GFDL and ECHAM/LSG runs than in the HadCM2 run, in which the Pacific overturning cell with the upwelling in the Tropics is essentially absent. In this sense, spectral characteristics are associated with the time-mean state of the deep ocean. For the northern North Atlantic, the northern North Pacific, and the Southern Ocean, the low-frequency slope β_l is close to zero for all four models, indicating white spectra over the low frequencies.

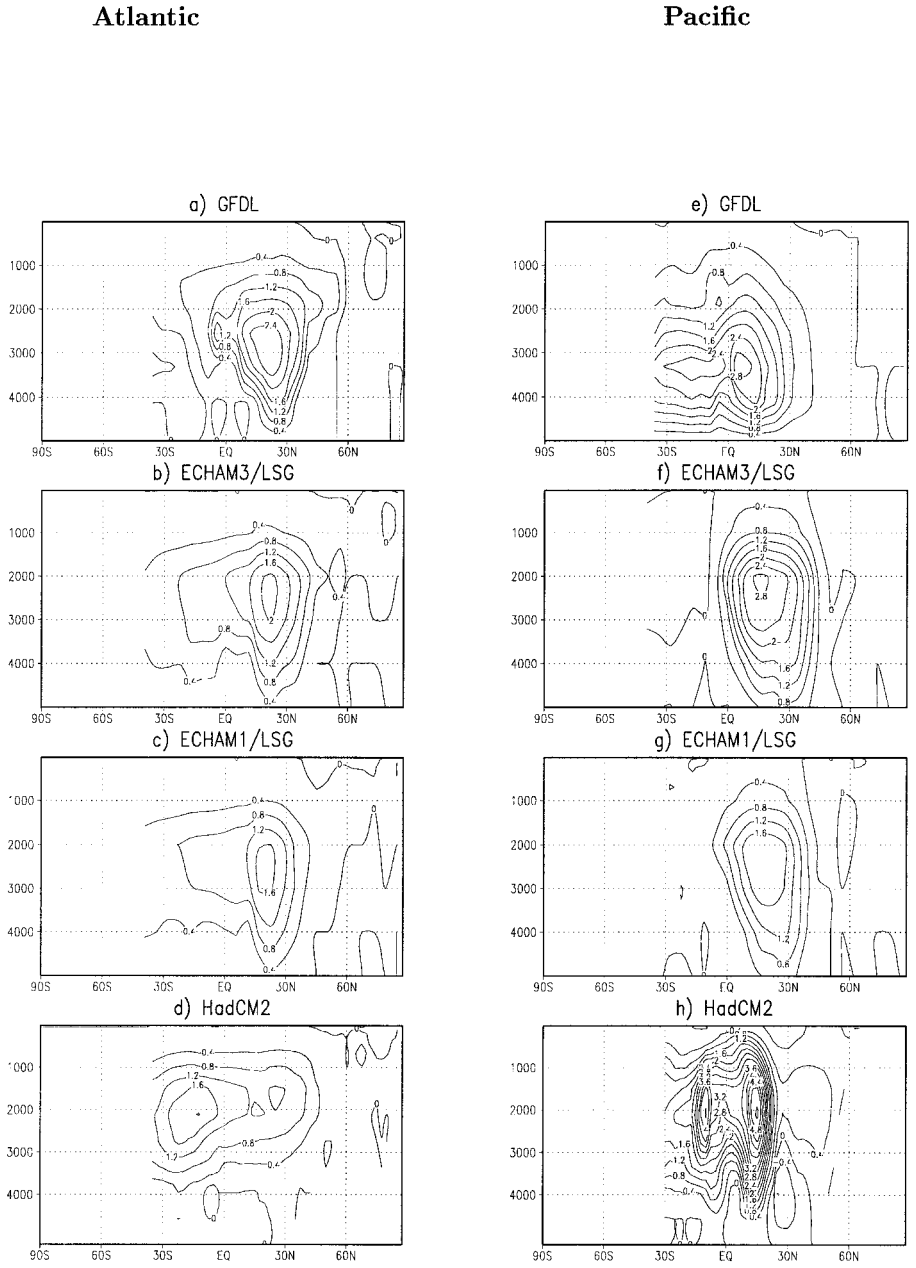

FIG. 16. EOF1 of zonally averaged and vertically weighted streamfunctions separately derived from data in the Atlantic, Pacific, and Indian Ocean. The weighting is defined such that the vertically integrated transport of the weighted data is identical to the vertically integrated transport of the unweighted data. The Atlantic EOFs in (a–d) explain, respectively, 56%, 41%, 51%, and 43%, and the Pacific EOFs in (e–h) explain, respectively, 51%, 33%, 35%, and 41% of the total variances.

Unlike β_l, the distributions of the slope β_h of the high-frequency spectrum in the four runs are more comparable to each other. Here β_h is close to zero in almost the entire Pacific. The high-frequency slope tends to be larger than one in the northern North Atlantic and in the Southern Ocean. In the subtropical Atlantic of the HadCM2 run, the values of β_h are larger than zero.

The fact that the spectra of mass transport can be approximated by (1) suggests that these spectra are continuous and do not have isolated maxima.

The estimated spectral power laws can be used to diagnose the underlying dynamics of the system. In particular, a spectrum with β_l being larger than zero implies a maximal memory timescale that is beyond the longest resolvable timescale. The analysis of spectral power laws indicates that the maximal memory timescale of deep tropical and subtropical water masses is longer than a few centuries, and that of water masses in the North Atlantic and North Pacific and in the Southern Ocean is about a few decades. To specify the maximal memory

TABLE 2. Zero-lag correlations between PC1/PC2 of the Atlantic (Atl.) streamfunctions and PC1/PC2 of the streamfunctions in the Pacific (Pac.) and the Indian Ocean, (Ind. Oc.) as calculated for the GFDL, ECHAM3/LSG, ECHAM1/LSG, and HadCM2 runs.

		PC1 (Pac.)	PC2 (Pac.)	PC1 (Ind. Oc.)	PC2 (Ind. Oc.)
GFDL	PC1 (Atl.)	−0.16	0.27	−0.28	−0.53
	PC2 (Atl.)	0.47	0.03	0.60	−0.17
ECHAM3/LSG	PC1 (Atl.)	0.03	−0.21	0.03	0.11
	PC2 (Atl.)	−0.19	−0.07	0.04	0.15
ECHAM1/LSG	PC1 (Atl.)	0.13	−0.06	−0.17	−0.01
	PC2 (Atl.)	−0.05	−0.04	−0.07	−0.12
HadCM2	PC1 (Atl.)	−0.03	0.06	−0.02	0.10
	PC2 (Atl.)	−0.25	0.14	−0.10	0.01

timescale of deep tropical and subtropical oceans and to describe variations up to this timescale, integrations over time periods longer than 1000 yr are required.

The dominant spatial features are derived from EOF analyses. For all four runs, the first EOFs are similar to each other. They are characterized by streamlines that tend to be closed within each ocean basin and describe recirculations of intermediate water masses within each ocean basin. The spatial scale of these modes is therefore smaller than that of the time-mean circulation. A consideration of lagged cross-correlation functions between PCs in different oceans indicates that because of the small equivalent sample size, the correlations between large-scale variations in different oceans may not be statistically significant.

The deep oceans considered in this paper are simulated with the first generation of the coupled atmosphere–ocean GCMs capable of being integrated over a time period of 1000 yr. Different time-mean circulations of the deep oceans are found. The differences may be induced by different formulations of the models, including different resolutions, but may also be induced by different spinup procedures. In any case, the statistical properties discussed in this paper crucially depend on the time-mean circulation. In particular, deep oceans with a well-defined overturning cell in the Pacific reveal more pronounced low-frequency variations. To what extent this generalized statement holds for other integrations is not clear. There is still much research to be performed to complete our knowledge about the variability of the present-day thermohaline circulation. This knowledge is especially important given that many models show a weakening of the thermohaline circulation in the Atlantic in response to increasing greenhouse gases in the atmosphere.

Acknowledgments. We thank Ernst Maier-Reimer for helpful discussions concerning the oceanic circulation. This work is supported by the EC under Grant ENV4-CT95-0101. The last author and the HadCM2 simulation are funded by Contract PECD 7/12/37/ from the U.K. Department of the Environment, Transport and the Regions.

REFERENCES

Broecker, W. S., 1991: The great ocean conveyor. *Oceanography,* **4,** 79–89.

Bryan, K., 1969: A numerical model for the study of the circulation of the World Ocean. *J. Comput. Phys.,* **3,** 347–376.

——, 1984: Accelerating the convergence to equilibrium of ocean climate models. *J. Phys. Oceanogr.,* **14,** 666–673.

Bryden, H. L., D. H. Roemmich, and J. A. Church, 1991: Ocean heat transport across 24°N in the Pacific. *Deep-Sea Res.,* **38,** 297–324.

Cox, M. D., 1984: A primitive equation, three dimensional model of the ocean. GFDL Ocean Group Tech. Rep. 1, 143 pp. [Available from Geophysical Fluid Dynamics Laboratory/NOAA, P.O. Box 308, Princeton, NJ 08542.]

Cubasch, U., K. Hasselmann, H. Höck, E. Maier-Reimer, U. Mikolajewicz, B. D. Santer, and R. Sausen, 1992: Time-dependent greenhouse warming computations with a coupled ocean–atmosphere model. *Climate Dyn.,* **8,** 55–69.

Delworth, T., S. Manabe, and R. J. Stouffer, 1993: Interdecadal variations of the thermohaline circulation in a coupled ocean–atmosphere model. *J. Climate,* **6,** 1993–2011.

Frankignoul, C., P. Müller, and E. Zorita, 1997: A simple model of the decadal response of the ocean to stochastic wind forcing. *J. Phys. Oceanogr.,* **27,** 1533–1546.

Gates, W. L., 1992: AMIP: The Atmospheric Model Intercomparison Project. *Bull. Amer. Meteor. Soc.,* **73,** 1962–1970.

Hasselmann, K., 1976: Stochastic climate models. Part I: Theory. *Tellus,* **28,** 473–485.

——, 1982: An ocean model for climate variability studies. *Progress in Oceanography,* Vol. 11, Pergamon, 69–92.

Johns, T. C., R. E. Carnell, J. F. Crossley, J. M. Gregory, J. F. B. Mitchell, C. A. Senior, S. F. B. Tett, and R. A. Wood, 1997: The second Hadley Centre coupled ocean–atmosphere GCM: Model description, spinup and validation. *Climate Dyn.,* **13,** 103–134.

Kraus, E. B., and J. S. Turner, 1967: A one dimensional model of the seasonal thermocline. Part II. *Tellus,* **19,** 98–105.

Maier-Reimer, E., U. Mikolajewicz, and K. Hasselmann, 1993: Mean circulation of the Hamburg LSG OGCM and its sensitivity to the thermohaline surface forcing. *J. Phys. Oceanogr.,* **23,** 731–757.

Manabe, S., and R. J. Stouffer, 1996: Low-frequency variability of surface air temperature in a 1000-year integration of a coupled atmosphere–ocean–land surface model. *J. Climate,* **9,** 376–393.

——, ——, M. J. Spelman, and K. Bryan, 1991: Transient responses of a coupled ocean–atmosphere model to gradual changes of atmospheric CO_2. Part I: Annual mean response. *J. Climate,* **4,** 785–818.

Rahmstorf, S., 1995: Bifurcations of the Atlantic thermohaline circulation in response to changes in the hydrological cycle. *Nature,* **378,** 145–149.

Roemmich, D. H., and C. Wunsch, 1985: Two transatlantic sections: Meridional circulation and heat flux in the subtropical North Atlantic Ocean. *Deep-Sea Res.,* **32,** 619–664.

Schmitz, W. J., Jr., 1995: On the interbasin-scale thermocline circulation. *Rev. Geophys.,* **33,** 151–173.

Tett, S. F. B., T. C. Johns, and J. F. B. Mitchell, 1997: Global and regional variability in a coupled AOGCM. *Climate Dyn.,* **13,** 303–323.

von Storch, J.-S., 1994: Interdecadal variability in a global coupled model. *Tellus,* **46A,** 419–432.

——, 1999: On the reddest atmospheric modes and the forcings of the spectra of these modes. *J. Atmos. Sci.,* **56,** 1614–1626.

——, V. Kharin, U. Cubasch, G. C. Hegerl, D. Schriever, H. von Storch, and E. Zorita, 1997: A description of a 1260-year control integration with the coupled ECHAM1/LSG general circulation model. *J. Climate,* **10,** 1526–1544.

Voss, R., 1996: Entwicklung eines Kopplungsverfahrens zur Reduzierung der Rechenzeit von Atmosphäre–Ozean Modellen. Examensarbeit 38, DKRZ, 123 pp. [Available from Deutsche Klimarechen Zentrum, Bundesstr. 55, D-20146 Hamburg, Germany.]

——, R. Sausen, and U. Cubasch, 1998: Periodically synchronously coupled integrations with the atmosphere–ocean general circulation model ECHAM3/LSG. *Climate Dyn.,* **14,** 249–266.

Zwiers, F. W., and H. von Storch, 1995: Taking serial correlation into account in tests of the mean. *J. Climate,* **8,** 336–351.